2017

SAR ground-plane mover signatures for non-zero radar ascent

Garren, David Alan

IEEE

D.A. Garren, "SAR ground-plane mover signatures for non-zero radar ascent," IEEE Transactions on Aerospace and Electronic Systems, (2017), 6 p.
http://hdl.handle.net/10945/56250

This article has been accepted for publication in a future issue of this journal, but has not been fully edited. Content may change prior to final publication. Citation information: DOI 10.1109/TAES.2017.2688898, IEEE Transactions on Aerospace and Electronic Systems

SAR Ground-Plane Mover Signatures for Non-Zero Radar Ascent

David Alan Garren, *Senior Member, IEEE*

***Abstract*—Recent spotlight synthetic aperture radar (SAR) analyses predict the two-dimensional (2D) range migration signature smears induced by targets with arbitrary motion in the ground-plane. These investigations were limited to constant-velocity radar motion with level flight path. The current correspondence removes this constraint by including the radar trajectory ascent angle.**

***Index Terms*—Synthetic aperture radar, radar signatures, moving targets.**

I. Introduction

Recent analyses [1]–[6] investigate spotlight SAR image signatures for ground-plane targets moving with arbitrary motion for cases in which the radar trajectory has constant velocity on a straight and level flight path. In particular, Ref. [1] determines the shape, extent, and position of the 2D central smear contour induced by a ground-plane target with arbitrary motion for zero radar trajectory squint angle. Refs. [5], [6] relax the constraint of zero squint angle. In addition, Ref. [5] predicts the 2D sructure of the mover signature, including the smear width and interference effects.

These signature prediction equations yield excellent agreement with detailed SAR simulations. However, SAR collections also can be applied for geometries with an ascending or descending radar trajectory [7]. The current investigation extends the prior studies by relaxing the constraint of a level flight path, so that the radar trajectory ascent angle relative to the ground-plane can be non-zero. There is no constraint on the three-dimensional (3D) orientation of the platform, since the radar mainbeam can be steered torwards the region of interest. The predictive signature capabilities of these analyses are valid for all SAR image formation methodologies [7]–[10].

Many studies [11]–[15] investigate various issues pertaining to SAR moving target signatures. Some researchers [16]–[18] analyze moving target phenomenology using power series expansions of the motion-induced phase error. Ref. [16] examines the signatures of constant velocity targets, which are related to range migration effects [19], [20]. Ref. [21] analyzes the signatures of piece-wise constant velocity targets for bistatic collection geometries. Other references are provided in Refs. [5], [6] and are not duplicated herein.

Section II gives the overall geometry and coordinates of the present analysis. Sections III and IV describe subaperture image computation and moving target smears, respectively. Section V compares the results with SAR numerical simulations. The conclusions are discussed in the final section.

D. A. Garren is with the Department of Electrical and Computer Engineering, Naval Postgraduate School, Monterey, CA, 93943 USA e-mail: dagarren@nps.edu

II. Geometry and Coordinates

Define a set of fixed 3D Cartesian coordinates with the origin $\{x, y, z\} = \{0, 0, 0\}$ lying at the ground-plane location at which the radar steers its mainbeam. This coordinate origin is the ground reference point (GRP). The coordinate z increases with altitude above the terrain, with $z = 0$ defining the ground-plane. The coordinate x increases with ground down-range from the radar at the collection midpoint. The ground cross-range coordinate y completes the right-handed coordinates.

The radar transmits for a duration of T_0 between $-T_0/2$ and $T_0/2$. During this interval, the target moves within the ground-plane according to two arbitrary analytic functions of slow-time t in the ground down-range x and ground cross-range y directions:

$$x = \alpha(t), \qquad y = \beta(t). \tag{1}$$

The current investigation extends prior analyses [1], [5], [6] for cases in which the radar trajectory has a non-zero radar trajectory ascent angle λ relative to the ground-plane, as well as that of a non-zero ground-plane squint angle φ_g. Figure 1 shows the definitions of λ and φ_g. In these graphics, the radar velocity vector $\mathbf{V_0}$ is decomposed into perpendicular $\mathbf{V}_\perp$ and parallel $\mathbf{V}_\parallel$ components relative to the ground-plane. It should be clarified that this radar trajectory ascent angle λ is not necessarily equal to the pitch angle of the radar platform fuselage relative to the ground-plane.

Define the following constant-velocity radar trajectory as a function of slow-time t:

$$X(t) = V_0\, t \sin(\varphi_g) \cos(\lambda) - X_0, \tag{2}$$

$$Y(t) = \pm V_0\, t \cos(\varphi_g) \cos(\lambda), \tag{3}$$

$$Z(t) = V_0\, t \sin(\lambda) + Z_0. \tag{4}$$

Here, V_0 is the constant radar speed. Also, X_0 and Z_0 are the ground down-range and altitude, respectively, relative to the ground reference point (GRP) at $t = 0$. The upper sign in (3) corresponds to a radar that is pointed to the right, and the lower sign corresponds to a radar pointing to the left.

The squint angle φ_g is defined from the broadside direction, such that positive values apply in the direction towards the radar velocity vector and negative angles imply the opposite direction. The ascent angle λ is defined so that a positive value gives a radar which is increasing in altitude, whereas a negative value implies a descending trajectory.

It is assumed that the platform steers the radar mainbeam towards the region on the ground to be imaged throughout the SAR collection. Such steering can be performed by either mechanical or electronic means. Thus, there is no need to

This article has been accepted for publication in a future issue of this journal, but has not been fully edited. Content may change prior to final publication. Citation information: DOI 10.1109/TAES.2017.2688898, IEEE Transactions on Aerospace and Electronic Systems

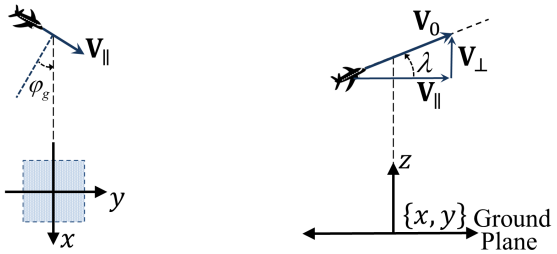

(a) (b)

Fig. 1. Collection geometry: (a) The top view shows the radar squint angle of φ_g relative to the ground-plane coordinates $\{x, y\}$; (b) The side view shows the radar trajectory ascent angle λ relative to the perpendicular $\mathbf{V}_{\perp}$ and parallel $\mathbf{V}_{\|}$ components of the radar velocity vector relative to the ground-plane. Also, z is the altitude above the ground-plane.

explicitly model the 3D orientation of the body of the radar platform with regards to the ground-plane.

Define the time-dependent azimuthal and elevation angles, respectively, of the instantaneous radar position relative to the GRP via [5]:

$$\varphi(t) \equiv \arctan\left(\frac{Y(t)}{X(t)}\right), \tag{5}$$

$$\theta(t) \equiv \arctan\left(\frac{Z(t)}{\sqrt{\{X(t)\}^2 + \{Y(t)\}^2}}\right). \tag{6}$$

The temporal frequency f is used to define the spatial frequency via $\rho \equiv 2f/c$, which facilitates the transformation from the spherical spatial frequency domain $\{\rho, \varphi, \phi\}$ to the Cartesian form [5]:

$$\xi(\rho, t) \equiv \rho \cos\big(\varphi(t)\big) \cos\big(\theta(t)\big), \tag{7}$$

$$\eta(\rho, t) \equiv \rho \sin\big(\varphi(t)\big) \cos\big(\theta(t)\big). \tag{8}$$

Here, ξ and η are equal to the down-range and cross-range components of the spatial frequency, respectively.

III. Subaperture Images

SAR imagery can be computed using [1], [5]:

$$b(x, y) \equiv \int_{\xi_0 - \Delta_\xi/2}^{\xi_0 + \Delta_\xi/2} d\xi \int_{-\Delta_\eta/2}^{\Delta_\eta/2} d\eta \; h(x, y, \xi, \eta), \tag{9}$$

in terms of the kernel function:

$$h(x, y, \xi, \eta) \equiv U(\xi, \eta)\, G(\xi, \eta) \exp\Big(j2\pi\{x\xi + y\eta\}\Big). \tag{10}$$

Here, the imaginary constant is $j = \sqrt{-1}$. In addition, ξ_0 is the central value of the ground down-range spatial frequency, and Δ_ξ and Δ_η are the full spatial frequency bandwidths in the down-range and cross-range directions, respectively. The function $G(\xi, \eta)$ gives the radar return data, and the factor $U(\xi, \eta)$ enables 2D weighting for sidelobe control.

The moving target signature contour follows the spatial locations of image energy deposition in the synthesis of (9), as applied by Jao [16]. Corresponding subaperture images [1], [5] can be computed via:

$$\tilde{b}_s(x, y) \equiv \int_{\xi_0 - \Delta_\xi/2}^{\xi_0 + \Delta_\xi/2} d\xi \int_{\eta_s - \delta_\eta/2}^{\eta_s + \delta_\eta/2} d\eta \; h(x, y, \xi, \eta). \tag{11}$$

Here, η_s is the central value of the cross-range spatial frequency for subaperture s.

IV. Analytic Predictions

Analytic prediction of moving target signatures requires the slow-time t in terms of ξ and η. The projection-slice theorem [7] implies that φ and ϕ of (5) and (6), respectively, of the 3D spatial coordinates $\{x, y, z\}$ are identical to that for the corresponding 3D spatial frequency coordinates $\{\xi, \eta, \zeta\}$, wherein ζ is the altitude spatial frequency. Thus, (5) has the following dual form:

$$\tan(\varphi) = \frac{Y(t)}{X(t)} = \frac{\eta}{\xi}. \tag{12}$$

Then, use of (2)-(4) gives:

$$\frac{\eta}{\xi} = \frac{\pm V_0 t \cos(\varphi_g)\cos(\lambda)}{V_0 t \sin(\varphi_g)\cos(\lambda) - X_0}. \tag{13}$$

Therefore, the slow-time t can be solved to yield:

$$t(\xi, \eta) = \frac{\kappa_0\, \eta}{\xi - \iota_0\, \eta}, \tag{14}$$

in terms of two constants parameters:

$$\kappa_0 \equiv \mp \frac{X_0}{V_0 \cos(\lambda)\cos(\varphi_g)}, \qquad \iota_0 \equiv \pm \tan(\varphi_g). \tag{15}$$

In addition, the mean value of the slow-time t for a particular subaperture s follows from (14), i.e.,

$$\tau_s \equiv \frac{\kappa_0\, \eta_s}{\xi_0 - \iota_0\, \eta_s}. \tag{16}$$

The previous analyses [5], [6] permit non-zero values for φ_g but require zero values for λ. Comparison of (15) with that of these prior investigations reveals that the primary modification is the introduction of the factor $1/\cos(\lambda)$ within the parameter κ_0. Therefore, the analytic results of Ref. [5] can be extended to apply for non-zero λ via the parameter κ_0 of (15).

Define the following parameters [5]:

$$\epsilon_s \equiv \frac{\eta - \eta_s}{\xi_0}, \qquad \kappa_s' \equiv \frac{\kappa_0}{1 - \iota_0\, \epsilon_s}. \tag{17}$$

The n^{th} order derivatives of the true target motion functions $\{\alpha(t), \beta(t)\}$ of (1) can be used to compute the corresponding $\{x, y\}$ components of the instantaneous target position $\{\mu_0(\tau_s), \nu_0(\tau_s)\}$ and velocity $\{\mu_1(\tau_s), \nu_1(\tau_s)\}$ via:

$$\mu_n(\tau_s) = \left.\frac{d^n \alpha(t)}{dt^n}\right|_{t=\tau_s}, \qquad \nu_n(\tau_s) = \left.\frac{d^n \beta(t)}{dt^n}\right|_{t=\tau_s}. \tag{18}$$

For the case of a uniform window in the frequency domain, the subapeture function (11) reduces to the form [5]:

$$\tilde{b}_s(x, y) = \sigma_0\, \Delta_\xi\, \delta_\eta \exp\Big(j2\pi\, \omega_{0,0}(x, y, \epsilon_s)\, \xi_0\Big) \times \operatorname{sinc}\left(\frac{\omega_{1,0}(x, \epsilon_s)\, \Delta_\xi}{1 - \iota_0\, \epsilon_s}\right) \operatorname{sinc}\left(\frac{\omega_{0,1}(y, \epsilon_s)\, \delta_\eta}{1 - \iota_0\, \epsilon_s}\right), \tag{19}$$

in terms of the following functions:

$$\omega_{0,0}(x, y, \epsilon_s) \equiv x - \mu_0\big(\tau(\epsilon_s)\big) + \Big\{y - \nu_0\big(\tau(\epsilon_s)\big)\Big\}\epsilon_s, \tag{20}$$

This article has been accepted for publication in a future issue of this journal, but has not been fully edited. Content may change prior to final publication. Citation information: DOI 10.1109/TAES.2017.2688898, IEEE Transactions on Aerospace and Electronic Systems

$$\omega_{1,0}(x,\epsilon_s) \equiv \Big\{x - \mu_0\big(\tau(\epsilon_s)\big)\Big\}\Big\{1 - \iota_0\,\epsilon_s\Big\} + \kappa_s'\,\mu_1\big(\tau(\epsilon_s)\big)\,\epsilon_s + \kappa_s'\,\nu_1\big(\tau(\epsilon_s)\big)\,\epsilon_s^2, \quad (21)$$

$$\omega_{0,1}(y,\epsilon_s) \equiv \Big\{y - \nu_0\big(\tau(\epsilon_s)\big)\Big\}\Big\{1 - \iota_0\,\epsilon_s\Big\} - \kappa_s'\,\mu_1\big(\tau(\epsilon_s)\big) - \kappa_s'\,\nu_1\big(\tau(\epsilon_s)\big)\,\epsilon_s. \quad (22)$$

This metholodology predicts that the central contour of the SAR signature induced by a ground-plane moving target for arbitrary λ and φ_g. This locus is the location of energy deposition for a given subaperture image $b_s(x,y)$, which corresponds to the maxima of the two sinc functions in (19). These maxima are obtained for zero values of the arguments of the two sinc functions, giving:

$$\omega_{1,0}(x,\epsilon_s) = 0, \qquad \omega_{0,1}(y,\epsilon_s) = 0. \quad (23)$$

The analysis proceeds by using (21) and (22) within (23) in order to solve for x and y:

$$x(\tau_s) = \mu_0(\tau_s) - \mu_1(\tau_s)\tau_s - \frac{1}{\kappa_0}\Big\{\nu_1(\tau_s) + \iota_0\mu_1(\tau_s)\Big\}\tau_s^2, \quad (24)$$

$$y(\tau_s) = \nu_0(\tau_s) + \kappa_0\mu_1(\tau_s) + \Big\{\nu_1(\tau_s) + 2\iota_0\mu_1(\tau_s)\Big\}\tau_s + \frac{1}{\kappa_0}\Big\{\iota_0\nu_1(\tau_s) + \iota_0^2\mu_1(\tau_s)\Big\}\tau_s^2. \quad (25)$$

These equations give the size, shape, and location of the central contour of the smear induced by the moving target.

V. Theory Validation

The theory equations for non-zero ascent and squint are validated via comparison with the mover smears resulting from the SAR image formation process applied to simulated radar measurements. For the following example, the radar moves with constant speed on a straight flight path, with an aft squint angle of $\varphi_g = -35^\circ$ off of the starboard side and a descending radar ascent angle of $\lambda = -20^\circ$. The following radar parameters are used in (2) – (4): speed $V_0 = 200\,\mathrm{m/s}$, ground down-range $X_0 = 30\,\mathrm{km}$, and altitude $Z_0 = 1\,\mathrm{km}$.

The radar transmits linear frequency modulated (LFM) chirp waveforms, e.g., [11], with center frequency $f_c = 1.5\,\mathrm{GHz}$, bandwidth $\Delta_f = 150\,\mathrm{MHz}$, and waveform duration $T_f = 150\,\mu\mathrm{s}$. Complex-valued I and Q data are measured over 1000 uniformly-spaced frequency samples. The radar transmits 5000 waveforms over the collection time of $T_0 = 15\,\mathrm{s}$. In addition, this model adds a statistically-independent, complex-valued Gaussian noise sample to each range bin [7]. For this example, the signal-to-noise ratio (SNR) of the range profile measurements is approximately $40\,\mathrm{dB}$.

A. Braking Target Motion

This example considers a constant-heading target that undergoes a braking maneuver according to the position profile [6]:

$$\alpha(t) = \alpha_0 + \cos(\phi_0)\Big\{v_0\,t + w_0\,\gamma_0\ln\Big(\cosh\big(\psi(t)\big)\Big)\Big\}, \quad (26)$$

$$\beta(t) = \beta_0 + \sin(\phi_0)\Big\{v_0\,t + w_0\,\gamma_0\ln\Big(\cosh\big(\psi(t)\big)\Big)\Big\}, \quad (27)$$

with $\psi(t) \equiv \{t - t_0\}/\gamma_0$. For this example, $\alpha_0 = 0\,\mathrm{m}$, $\beta_0 = 0\,\mathrm{m}$, $v_0 = 13\,\mathrm{m/s}$, $w_0 = -1\,\mathrm{m/s}$, and $\gamma_0 = 0.5\,\mathrm{s}$. This target trajectory is shown in Figure 2(a), with circles at 3-second intervals. The overall context of the target and radar is presented in Figure 2(b). Finally, The target speed is shown in Figure 2(c).

Figure 3(a) presents the 2D struction of the signature smear induced by the braking target. For this figure and those that follow, the down-range axis is stretched relative to that in the cross-range dimension in order to clarify the detailed smear structure. In addition, this figure includes an overlay of the predictied signature contour. The specific location, extent, and shape of the predicted central contour is obtained by using (24) and (25), with the required derivatives of (18) obtained from (26) and (27). The resulting trace of the central contour is overlaid onto the Polar Format Algorithm (PFA) [7], [10] image formation result in Figure 3(a). Clearly, the predictions provide excellent agreement with the smear in terms of location, extent, and shape.

Further insight is obtained by using (19) to coherently sum a large number of non-overlapping subaperture IPRs. Figure 3(b) applies 128 IPRs, with an overlay of the predicted central contour. The coherent synthesis in Figure 3(b) agrees well with the image formation smear of Figure 3(a) in terms of location, extent, and shape. In addition, there is good agreement in terms of the smear width and the self-interference structure.

Figure 4(a) presents the results of $\lambda = -40^\circ$, with all other parameters identical to that of the $\lambda = -20^\circ$ case. The $\lambda = -40^\circ$ smear does not cross itself, unlike the case of $\lambda = -20^\circ$, as explained later in this section.

It is interesting to compare these results with the $\lambda = 0^\circ$ case of a level flight path, as shown in Figure 4(b). This $\lambda = 0^\circ$ signature more closely matches the $\lambda = -20^\circ$ case than does the result for $\lambda = -40^\circ$. This apparent disparity is due to the $1/\cos(\lambda)$ factor in geometric constant κ_0 of (15).

It should be clarified that κ_0 of (15) has the same value if the sign of λ is changed, i.e., $\lambda \to -\lambda$. Thus, an ascending radar ascent angle of $\lambda = 20^\circ$ gives the same result as Figure 3(a), as is confirmed with direct simulation. In addition, the $\lambda = 40^\circ$ case can be verified via simulation to give the same result as that of Figure 4(a).

The reciprocal of the κ_0 has the units of inverse time and can be understood as an angular rotation rate of the radar relative to the scene to be imaged. Thus, the introduction of a non-zero λ serves to decrease the effective sensor rotation rate by a factor of $\cos(\lambda)$. Thus, it is interesting to examine the effect of increasing the total collection time by the factor $1/\cos(\lambda)$ in order to counteract this decreased effective rotation rate.

Figure 5 examines the case of $\lambda = -40^\circ$ with an increased total collection time to be $T_0 = 15\,\mathrm{s}/\cos(-40^\circ)$ while keeping all other parameters fixed. This figure reveals that the basic shape of the smear is identical to that of the zero-ascent case of Figure 4(b), except that the overall extent is increased by the factor $1/\cos(\lambda)$. This result is consistent with the increase in the extent of by $1/\cos(\lambda)$ via the linear τ_s term in (25). In addition, the cross-range offset of the smear relative to truth is also increased by the factor $1/\cos(\lambda)$, which is consistent with the $\kappa_0\mu_1(\tau_s)$ term in (25).

This article has been accepted for publication in a future issue of this journal, but has not been fully edited. Content may change prior to final publication. Citation information: DOI 10.1109/TAES.2017.2688898, IEEE Transactions on Aerospace and Electronic Systems

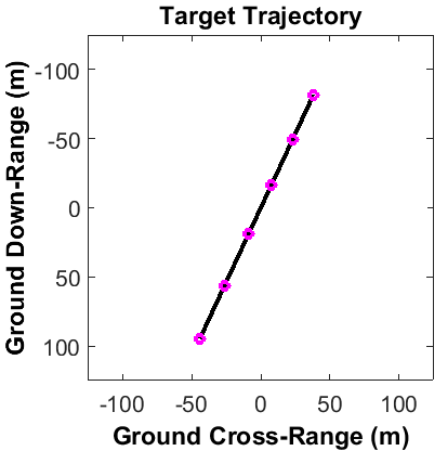

(a)

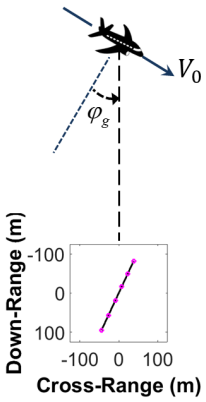

(b)

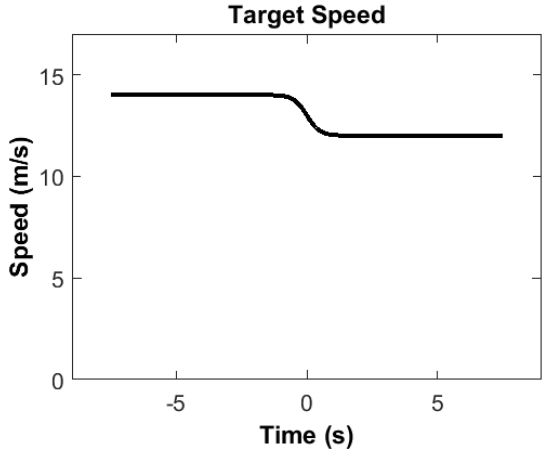

(c)

Fig. 2. True target motion: (a) Braking target trajectory in the ground-plane, with circles at 3-second intervals; (b) Overall context of the target trajectory with regard to the radar trajectory; and, (c) Target speed as a function of slow-time.

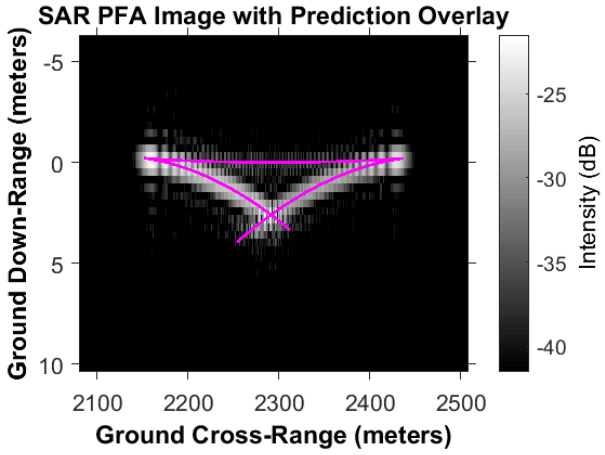

(a)

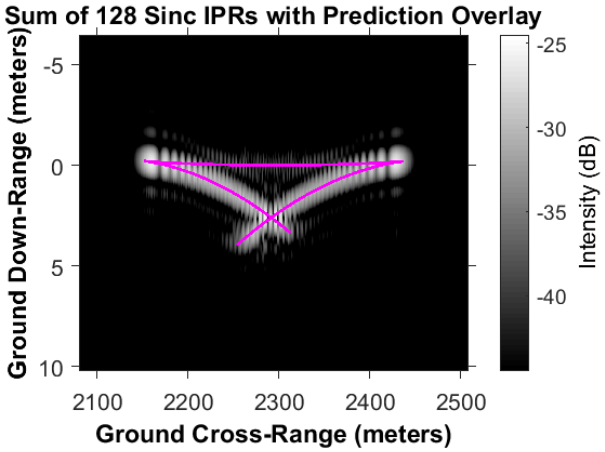

(b)

Fig. 3. Prediction of the location, extent, and shape of the smear induced by braking target motion for $\lambda = -20°$ and $\varphi_g = -35°$: (a) SAR PFA image with an overlay of the predicted central contour of the target signature; (b) Coherent summation of 128 sinc IPR functions corresponding to non-overlapping subapertures, with an overlay of the predicted central contour of the target signature.

The reader can glean additional insight via an approximation of the target motion in Figure 2. Specifically, assume that Figure 2(c) corresponds approximately to that of a constant-velocity target with speed v_0 for the initial 7 seconds, followed by a period of constant deceleration with magnitude $\Delta_v/\{1\,\mathrm{sec}\}$ for the next second. The final 7-sec portion is that of a constant-velocity target with a lower speed of $v_0 - \Delta_v$.

The constant-velocity segment corresponding to the initial 7 seconds yields a parabolic shape. However, the target is executing this particular speed for only approximately one-half of the total collection time, so that only about one-half of the full parabola is produced in the signature. The specific values of this first constant-velocity segment determine the parabolic apex location and half-width via (24)-(25), as well as the particular side of the parabola. The third motion segment corresponding to the lower speed gives the other half-parabola.

The transition from the initial constant-velocity motion segment to the latter occurs over the relatively short time interval of 1 second. Thus, there is relatively little time for any significant range migration to occur. Therefore, an

This article has been accepted for publication in a future issue of this journal, but has not been fully edited. Content may change prior to final publication. Citation information: DOI 10.1109/TAES.2017.2688898, IEEE Transactions on Aerospace and Electronic Systems

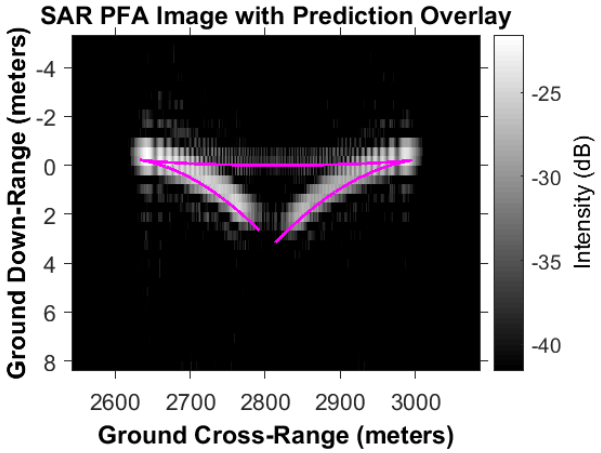

(a)

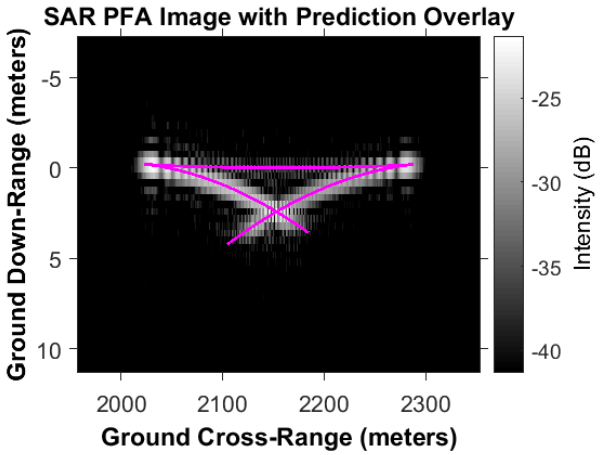

(b)

Fig. 4. SAR PFA images for braking target motion with prediction overlays for other values of λ: (a) The case of $\lambda = -40°$ and $\varphi_g = -35°$; (b) The case of $\lambda = 0°$ and $\varphi_g = -35°$.

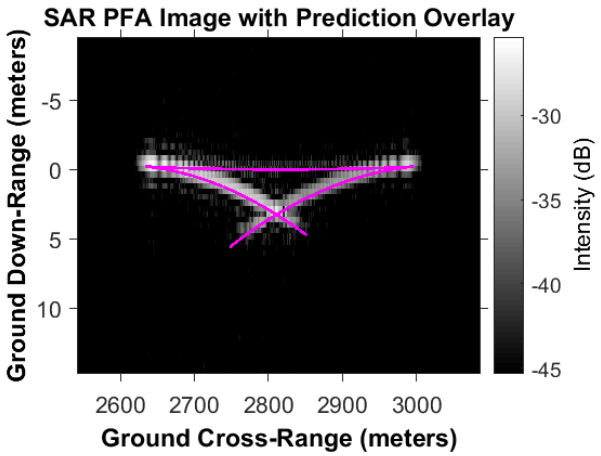

Fig. 5. The effects of increasing the total collection interval by a factor of $1/\cos(\lambda)$: SAR PFA image with prediction overlay for the case of $\lambda = -40°$ and $\varphi_g = -35°$, but with the total collection interval increased by a factor of $1/\cos(\lambda)$.

approximate straight line connects the apexes of the two half-parabolas. The relatively short duration of this speed transition also implies that there is less imagery energy deposited, so that the intensity is reduced in comparison to the two half-parabolas of the signature.

The larger ascent angle example of Figure 4(a) yields an interesting signature in which the two half-parabolas do not cross. This result follows since the two half-parabolas that are obtained from (24)-(25) give a separation between the parabolic apexes which is greater than the sum of the two half-parabola widths. In constrast, the zero-ascent angle case of Figure 4(b) yields a separation between the parabolic apexes which is less than the sum of the two half-parabola widths.

The specific collection parameters determine the value of κ_0 of (15), which then drives the signature contours per (24)-(25). The value of $|\lambda|$ gives a corresponding increase in $|\kappa_0|$ via the $1/\cos(\lambda)$ dependence. In addition, a larger $|\kappa_0|$ yields an increased cross-range offset via the $\kappa_0 \mu_1(\tau_s)$ term in (25), which gives an increased separation between the apexes of the half-parabolas. For Figure 4(a), this apex separation is sufficiently large that the half-parabolas no longer intersect.

B. Turning Target Motion

The second example is based upon a target that is executing a turning maneuver, as described via [6]:

$$\alpha(t) = \alpha_0 \mp \rho_0 \sin(\phi_0) \pm \rho_0 \sin\big(\omega(t)\big), \tag{28}$$

$$\beta(t) = \beta_0 \pm \rho_0 \cos(\phi_0) \mp \rho_0 \cos\big(\omega(t)\big), \tag{29}$$

wherein the phase angle $\omega(t)$ is defined by:

$$\omega(t) \equiv \pm \frac{v_0 t}{\rho_0} + \phi_0. \tag{30}$$

The parameters $\{\alpha_0, \beta_0, v_0, \rho_0, \phi_0\}$ determine the specific target motion. The upper signs in (28) and (29) correspond to a target that is turning to the left, and the lower signs give turning motion to the right.

These examples apply the following: $\alpha_0 = 0.0\,\mathrm{m}$, $\beta_0 = 0.0\,\mathrm{m}$, $v_0 = 13\,\mathrm{m/s}$, $\phi_0 = 155°$, and $\rho_0 = 500\,\mathrm{m}$. Figure 6(a) presents the true target trajectory corresponding to turning motion to the left. The radar mainbeam is aimed starboard at $\varphi_g = -35°$. The radar parameters are that of Figures 3(a), corresponding to $\lambda = -20°$. The prediction contour of Figure 6(b) reveals good agreement with the SAR image formation smear.

VI. Conclusion

This paper generates the signature morphology of ground-plane targets that can have arbitrary motion in spotlight SAR imagery for cases in which the radar trajectory has an arbitrary orientation relative to the ground-plane. That is, both the radar trajectory ascent angle relative to the ground-plane and the squint angle relative to broadside are permitted to be non-zero. Various examples demonstrate that the signature prediction equations yield excellent agreement with simulations. This investigation reveals that a "family" of moving target smears can have the same shape but possibly different cross-range extents and offsets, as obtained by scaling the reciprocal of the cosine of the radar trajectory ascent angle.

This article has been accepted for publication in a future issue of this journal, but has not been fully edited. Content may change prior to final publication. Citation information: DOI 10.1109/TAES.2017.2688898, IEEE Transactions on Aerospace and Electronic Systems

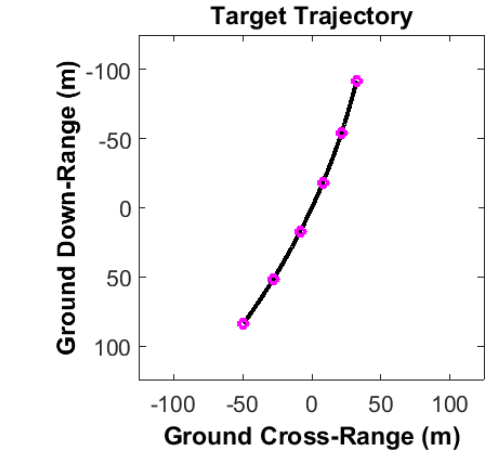

(a)

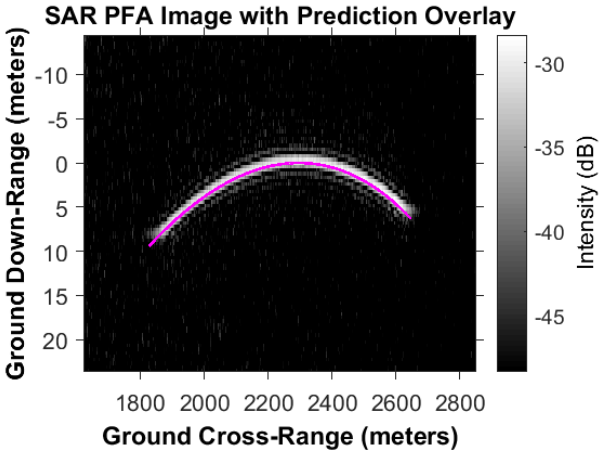

(b)

Fig. 6. SAR PFA image with prediction overlay for turning target motion and $\lambda = -20°$ and $\varphi_g = -35°$: (a) True target trajectory corresponding to turning motion to the left witb constant speed; and (b) Signature smear from SAR simulation with prediction overlay.

This methodology yields the moving target signature as a sum of sub-aperture sinc functions for cases in which both the radar ascent and squint angles are permitted to be non-zero. These detailed signature effects can provide insight into the underlying target motion characteristics that occurred during a given SAR collection. For example, parabolic or hyperbolic signature shapes often indicate uniform target motion. The present theory predicts the detailed smear morphology effects resulting from SAR collections with actual measured data.

ACKNOWLEDGMENT

The author thanks AFRL for partial support of this work. The author also thanks the anonymous reviewers for valuable suggestions. DoD Distribution Statement A: Unlimited Distribution. The views expressed in this document are those of the author and do not reflect the official policy or position of the Department of Defense or the U.S. Government.

REFERENCES

[1] D. A. Garren, "Smear signature morphology of surface targets with arbitrary motion in spotlight synthetic aperture radar imagery," *IET Radar, Sonar and Navigation*, vol. 8, no. 5, pp. 435–448, Jun 2014.

[2] ——, "Signatures of braking surface targets in spotlight synthetic aperture radar," *Proceedings of 2014 Sensor Signal Processing for Defence, held in Edinburgh, UK, on 08-09 September 2014*, pp. 51–55, Sep 2014.

[3] ——, "Signature predictions of surface targets undergoing turning maneuvers in spotlight synthetic aperture radar imagery," *Proceedings of SPIE, Vol. 9475, 94750A, Algorithms for Synthetic Aperture Radar Imagery XXII, 20 - 24 April 2015, in Baltimore, Maryland, USA*, pp. 4997–5008, Apr 2015.

[4] ——, "Signatures of surface targets with increasing speed in spotlight synthetic aperture radar," *2015 IEEE International Radar Conference, 11-15 May 2015 in Arlington, Virginia, USA*, p. 1114 1118, May 2015.

[5] ——, "Theory of two-dimensional signature morphology for arbitrarily moving surface targets in squinted spotlight synthetic aperture radar," *IEEE Transactions on Geoscience and Remote Sensing, Date of Publication to IEEE Xplore as an Early Access Article: 17 April 2015*, vol. 53, no. 9, pp. 4997–5008, Sep 2015.

[6] ——, "Signature morphology effects of squint angle for arbitrarily moving surface targets in spotlight synthetic aperture radar," *IEEE Transactions on Geoscience and Remote Sensing, Date of Publication to IEEE Xplore as an Early Access Article: 29 June 2015*, vol. 53, no. 11, pp. 6241–6251, Nov 2015.

[7] C. V. Jakowatz Jr., D. E. Wahl, P. H. Eichel, D. C. Ghiglia, and P. A.Thompson, *Spotlight-Mode Synthetic Aperture Radar: A Signal Processing Approach*. Norwell, MA, USA: Kluwer Academic Publishers, 1996.

[8] D. C. Munson, Jr., J. D. O'Brien, and W. K. Jenkins, "A tomographic formulation of spotlight-mode synthetic aperture radar," *Proceedings of the IEEE*, vol. 71, no. 8, pp. 917–925, 1983.

[9] J. L. H. Webb and D. C. Munson, Jr., "SAR image reconstruction for an arbitrary radar path," *1995 International Conference on Acoustics, Speech, and Signal Processing in Detroit, MI, on 09 May 1995 - 12 May 1995*, vol. 4, pp. 2285–2288, May 1995.

[10] W. G. Carrara, R. S. Goodman, and R. M. Majewski, *Spotlight Synthetic Aperture Radar Signal Processing Algorithms*. Norwood, MA, USA: Artech House, 1995.

[11] R. P. Perry, R. C. DiPietro, and R. L. Fante, "SAR imaging of moving targets," *IEEE Transactions on Aerospace and Electronic Systems*, vol. 35, no. 1, pp. pp. 188–200, Jan 1999.

[12] J. R. Fienup, "Detecting moving targets in SAR imagery by focusing," *IEEE Transactions on Aerospace and Electronic Systems*, vol. 37, no. 3, pp. 794–809, Jul 2001.

[13] D. Cristallini, D. Pastina, F. Colone, and P. Lombardo, "Efficient detection and imaging of moving targets in SAR images based on chirp scaling," *IEEE Transactions on Geoscience and Reomote Sensing*, vol. 51, no. 4, pp. 2403–2416, Apr 2013.

[14] C. V. Jakowatz Jr., D. E. Wahl, and P. H. Eichel, "Refocus of constant velocity moving targets in synthetic aperture radar imagery," *Proc. SPIE: Algorithms for Synthetic Aperture Radar Imagery V, Edmund G. Zelnio, Editor.*, vol. 3370, pp. 85–95, Apr 1998.

[15] M. Kirscht, "Detection and imaging of arbitrarily moving targets with single-channel SAR," *IEE Proceedings - Radar, Sonar, and Navigation*, vol. 150, no. 1, pp. 7–11, Feb 2003.

[16] J. K. Jao, "Theory of synthetic aperture radar imaging of a moving target," *IEEE Transactions on Geoscience and Remote Sensing*, vol. 39, no. 9, pp. 1984 –1992, Sep 2001.

[17] D. A. Garren, "Method and system for developing and using an image reconstruction algorithm for detecting and imaging moving targets," Patent US 7 456 780 B1, Nov 25, 2008.

[18] R. Linnehan, L. Perlovsky, C. Mutz, and J. Schindler, "Detecting slow moving targets in SAR images," *Proceedings of SPIE 5410, Radar Sensor Technology VIII and Passive Millimeter-Wave Imaging Technology VII, 64 (August 12, 2004)*, vol. 64, Aug 2004.

[19] R. H. Stolt, "Migration by fourier transform," *Geophysics*, vol. 43, pp. 23–48, 1978.

[20] S. Rahman, "Focusing moving targets using range migration algorithm in ultra wideband low frequency synthetic aperture radar," Master's thesis, Blekinge Institue of Technology, Jun 2010.

[21] K. Duman and B. Yazici, "Moving target artifacts in bistatic synthetic aperture radar images," *IEEE Transactions on Computational Imaging*, vol. 1, no. 1, pp. 30–43, Mar 2015.